



City Research Online

City, University of London Institutional Repository

Citation: Zhu, H., Crabb, D. P., Schlottmann, P. G., Lemij, H. G., Reus, N. J., Healey, P. R., Mitchell, P., Holm, T. & Garway-Heath, D. F. (2010). Predicting visual function from the measurements of retinal nerve fiber layer structure. *Investigative Ophthalmology and Visual Science*, 51(11), pp. 5657-5666. doi: 10.1167/iovs.10-5239

This is the unspecified version of the paper.

This version of the publication may differ from the final published version.

Permanent repository link: <https://openaccess.city.ac.uk/id/eprint/3332/>

Link to published version: <https://doi.org/10.1167/iovs.10-5239>

Copyright: City Research Online aims to make research outputs of City, University of London available to a wider audience. Copyright and Moral Rights remain with the author(s) and/or copyright holders. URLs from City Research Online may be freely distributed and linked to.

Reuse: Copies of full items can be used for personal research or study, educational, or not-for-profit purposes without prior permission or charge. Provided that the authors, title and full bibliographic details are credited, a hyperlink and/or URL is given for the original metadata page and the content is not changed in any way.

City Research Online:

<http://openaccess.city.ac.uk/>

publications@city.ac.uk

Predicting Visual Function from the Measurements of Retinal Nerve Fibre Layer Structure

Haogang Zhu,¹ David P Crabb,¹ Patricio G Schlottmann,² Hans G Lemij,³ Nicolaas J Reus,³ Paul R Healey,⁴ Paul Mitchell,⁴ Tuan Ho,² David F Garway-Heath²

¹Department of Optometry and Visual Science, City University London, United Kingdom

²NIHR Biomedical Research Centre for Ophthalmology, Moorfields Eye Hospital NHS Foundation Trust and UCL Institute of Ophthalmology, London, UK

³Glaucoma Service, The Rotterdam Eye Hospital, Rotterdam, Netherlands

⁴Department of Ophthalmology, University of Sydney, Sydney, Australia

Running Title: Zhu et al. Predict Visual Function from Retinal Structure

Key words: glaucoma, visual field, scanning laser polarimetry, Bayesian methodology, radial basis function, structure-function relationship

Corresponding author: David Crabb, Department of Optometry and Visual Science, City University London, Northampton Square, London, EC1V 0HB, UK. Phone: +44 (0) 2070400191; E-mail: d.crabb@city.ac.uk

Support: This research has been supported by Pfizer with an Investigator Initiated research grant; and has received a proportion of its funding from the Department of Health's NIHR Biomedical Research Centre for Ophthalmology at Moorfields Eye Hospital and UCL Institute of Ophthalmology. The views expressed in the publication are those of the authors and not necessarily those of the Department of Health.

Word Count: 6456 including appendix

Abstract

Purpose: To develop and validate a method for predicting visual function from retinal nerve fibre layer (RNFL) structure in glaucoma.

Methods: RNFL thickness (RNFLT) measurements from GDxVCC scanning laser polarimetry (SLP) and visual field (VF) sensitivity from standard automated perimetry were made available from 535 eyes from three centres. In a training dataset, structure-function relationships were characterized using linear regression and a type of neural network: Radial Basis Function customised under a Bayesian framework (BRBF). These two models were used in a test dataset to 1) predict sensitivity values at individual VF locations from RNFLT measurements and 2) predict the spatial relationship between VF locations and positions at a peripapillary RNFLT measurement annulus. Predicted spatial relationships were compared with a published anatomical structure-function map.

Results: Compared with linear regression, BRBF yielded a nearly two-fold improvement ($P < 0.001$; paired t-test) in performance of predicting VF sensitivity in the test dataset (mean absolute prediction error of 2.9dB (standard deviation (SD) 3.7dB) versus 4.9dB (SD 4.0dB)). The predicted spatial structure-function relationship accorded better ($P < 0.001$; paired t-test) with anatomical prior knowledge when the BRBF was compared with the linear regression (median absolute angular difference of 15° versus 62°).

Conclusions: The BRBF generates clinically useful relationships that relate topographical maps of RNFL measurement to VF locations and allows the VF sensitivity to be predicted from structural measurements. This method may allow clinicians to evaluate structural and functional measures in the same domain. It could also be generalized to use other structural measures.

Introduction

Assessing the way in which structural and functional measures in glaucoma interact is clinically important. Visual loss is assumed to follow from, and correlate to, structural loss caused by the disease process. It would be clinically useful to know the magnitude and location of structural loss that will result in visually important functional loss. However, current clinical devices for measuring structural and functional deficits are far from accurate and have imperfect precision. Structural measures of optic nerve head (ONH) topography or retinal nerve fibre layer thickness (RNFLT) can be made using optical imaging techniques, but these only provide surrogate measures of the biological variable of real interest, namely retinal ganglion cell (RGC) count and function. At the same time, standard automated perimetry (SAP), the clinical cornerstone of functional testing in glaucoma, is subject to considerable measurement variability and is also a poor surrogate for RGC count and function.¹ Despite their limitations, these techniques are currently central to the diagnosis and management of glaucoma. It would, therefore, be beneficial if structure and function measurements were directly linked in some way, allowing clinicians to corroborate decisions by considering the measurements in tandem.

There have been several studies attempting to quantify the structure-function relationship using clinical measurements. These typically proceed by taking one summary value to represent function (for example Mean Deviation, MD, of the visual field from SAP) and one number to represent the structural data (for example, average neuroretinal rim area or mean RNFLT), then simply assessing the curve linear (e.g. log-linear) or monotonic association between the two variables via R^2 , Pearson or Spearman coefficients.²⁻⁵ This approach suffers from two major flaws: the use of summary data loses spatial information and may reduce power, and these association measures and regression models assume a particular shape of the relationship. Furthermore these analyses fail to take account of spatial associations in the data, an integral attribute of glaucomatous loss.

While some studies have attempted to overcome these limitations by analysing smaller regions from the structural measures (for example, sectoral values of rim area) and groups or individual points in the visual field (VF),⁶⁻¹² we propose that much more could be gained by analysing the data in its 'high resolution form'. For example, in scanning laser polarimetry (SLP), RNFLT estimates are yielded over an image space of several thousand pixels; this is high-dimensional data and any method linking structural measures to the 50 or so individual points in the VF ideally should take this into account. Moreover, individual points from both

structure (pixel or sector values) and function (areas of VF or individual locations) are more likely to interact as ‘groups’ rather than single independent measurements.

In recent years, a special class of artificial neural networks using Radial Basis Functions (RBF) have received considerable attention.¹³⁻¹⁶ This class of networks differs from the artificial neural networks (ANNs) that use a multilayer perceptron (MLP) approach, in that the nonlinearity of the model is embedded in a hidden layer of the network: this hidden layer consists of basis functions. The key element of the RBF is that predictions can be made in a multi-dimensional space that consists of ‘mini-distributions’ of possible predictions, analogous to a kernel or window when interpolating data. RBF networks are particularly useful when mapping two- or three-dimensional images where interpolation is a prerequisite, with some image features being preserved while others not necessarily being mapped exactly. In this way they seem most suitable to the problem of mapping the individual points from the structural and functional measures. Moreover, the RBF method developed for our purposes is formulated under a Bayesian probabilistic framework in order to tackle the considerable variability in measurements as well as to form an automatic learning process: this customisation leads to what we denote a Bayesian RBF (BRBF) network.

The purpose of this study is to develop a general statistical method for linking clinically used measures of structure and function. We demonstrate the use of the method on measurements of the RNFLT derived from SLP with variable corneal compensation (GDxVCC) and individual visual field (VF) locations from SAP with the aim of providing predictions of one measure from another and to generate a topographical map of the spatial relationship between the imaged structure data and individual points in the visual field. It is imperative that any new method should be developed and tested on more than one data set: for this work we use three large data sets collected at three independent clinical centres. The method, which aims to make predictions, is compared to the correlation approach for mapping structural and functional measures typified by Gardiner and colleagues⁹ and we illustrate how the method can be extended to high resolution measurements.

Methods

Subjects

The study sample was derived from three independently acquired populations from Moorfields Eye Hospital, London (MEH), Rotterdam Eye Hospital, the Netherlands (REH) and the Blue Mountains Eye Study, Australia (BMES)

Moorfields Eye Hospital (MEH) Data

Thirty-four healthy subjects (34 eyes), 43 glaucomatous patients (43 eyes) and 30 ocular hypertension subjects (30 eyes) were enrolled. Inclusion criteria for the healthy subjects were a normal VF, intraocular pressure (IOP) <21 mm Hg, no previous history of ocular disease, and no family history of glaucoma in a first degree relative. For the glaucomatous patients, inclusion criteria were previously raised IOP (>21mmHg), reproducible VF defects and absence of other disorders that might cause VF loss. The VF defects were defined as a defect of two or more contiguous points in the Humphrey pattern deviation probability maps with P <1% loss or greater, or three or more contiguous points with P <5% loss or greater, or a 10 dB difference across the nasal horizontal midline at two or more adjacent points in the total deviation plot. Ocular Hypertension subjects were recruited from clinic on having a raised IOP >21 mmHg in two consecutive visits and having at least two normal VFs. Optic disc appearance was not used to categorize subjects. However, the optic disc was evaluated to exclude anatomical abnormalities such as coloboma or drusen. For all participants, one eye was randomly selected for study if both were eligible. All subjects had visual acuity of 20/40 or better, with ametropia <7 diopters, and had no other significant ocular abnormality or concomitant ophthalmic condition.

Rotterdam Eye Hospital (REH) Data

Forty six healthy subjects (46 eyes) and 76 glaucomatous patients (76 eyes) took part in a study that has been described in detail in Reus and Lemij (2005)¹⁷. In short, healthy subjects had normal VF, optic discs without structural abnormalities, IOP <21 mmHg, no previous history of ocular disease, and no family history of glaucoma. The patients had a glaucomatous appearance of the optic disc and a corresponding nerve fibre bundle VF defect, as described by Keltner et al. (2003)¹⁸ with SAP. All subjects had a visual acuity of 20/40 or better, and had no other significant ocular abnormality. For all participants, one eye was randomly selected for the study.

Blue Mountains Eye Study (BMES) Data

VFs and images were available for 1540 subjects from a large population-based study of visual impairment, common eye diseases, and other health conditions from an elderly community in Australia. A description of the Blue Mountain Eye Study (BMES) is given elsewhere.¹⁹ Two hundred and thirty healthy subjects (230 eyes) and 76 patients (76 eyes) diagnosed with glaucomatous optic neuropathy were selected from this population under strict measurement quality criteria (described below). Only one randomly selected eye per subject was used throughout. The criteria used for defining glaucomatous VF loss was an abnormal Humphrey Glaucoma Hemifield Test (GHT) plus one or more of the following VF defect classifications (top row of test points in 24-2 pattern were excluded to reduce the effect of lid artefact), which could not be explained on the basis of non-glaucomatous ocular, or neurological, causes: (1) at least 4 contiguous points on pattern deviation plot depressed at $p < 0.5\%$ level; (2) at least two horizontal points in nasal step locations with pattern deviation plot depressed at $p < 0.5\%$ level; (3) advanced glaucomatous field loss (hemispheric or severe generalised field loss, with residual temporal or central islands). Glaucoma was diagnosed if glaucomatous VF loss was present, combined with matching neural rim loss at the optic disc, and gonioscopy showed no evidence of angle-closure, rubeosis or secondary glaucoma, other than pseudoexfoliation syndrome.

All three datasets were collected in accordance with the tenets of the Declaration of Helsinki from studies that had local research ethics committee approval with all participants giving informed consent. Data were anonymized and transferred to a secure database held at City University London.

Measurements and Data

This study made use of measurements of the RNFL yielded from GDxVCC SLP (Carl Zeiss Meditec AG, Jena, Germany) and individual VF locations from SAP. The principles of SLP have been described by Greenfield et al (2003).²⁰ This instrumentation estimates the thickness of the peripapillary RNFLT by measuring the summed retardation in a polarized scanning laser beam reflected from the fundus. Retardation measurements at various points around the optic disc are used to construct a thickness map of the RNFL in micrometers. SLP with variable corneal compensation (VCC) has been shown to improve the estimates of RNFL thickness compared to earlier versions of the technology.²¹ All GDxVCC images, from all three centres, had quality scores greater than or equal to 8 and typical scan scores greater than or equal to 80. Single GDxVCC images were available from all the subjects from all the

centres. The 64-sector thickness profile on the peripapillary annulus (provided by the GDx software) for each subject and the raw images (.mif files) were transferred to a secure database.

The VF measurements were acquired in all cases using a Humphrey Field Analyzer (HFA) II (Carl Zeiss Meditec, CA, USA) using either full-threshold testing or the Swedish Interactive Threshold Algorithm (SITA) Standard test program in the standard 24-2 test pattern. For the MEH and REH data, all VFs were considered reproducible as well as reliable. The VFs from MEH data were all tested with the SITA standard program. VF reliability indices applied were: fixation losses $\leq 15\%$; and false-positive and false-negative response rates $\leq 25\%$. In the REH data, 29 healthy subjects and 73 glaucomatous subjects were tested with the full-threshold program and the others with the SITA standard program. Reliability indices applied were: fixation losses $\leq 25\%$; and false-positive and false-negative response rates $\leq 20\%$ for full-threshold test and $\leq 7\%$ for SITA standard test. Higher false-negative response rates were accepted in eyes with advanced field loss (up to 33%). All VFs in BMES were tested with the full-threshold program. Stricter reliability criteria were applied: fixation loss, false positive and false negative all $\leq 15\%$. In all eyes, the two VF test points above and below the blind spot were excluded and the remaining 52 raw (dB) sensitivity values (dB) were transferred to a secure database for analysis.

In this study, the MEH and REH datasets (229 eyes in total) were used for development of the models, and the BMES dataset (306 eyes in total) was used for independent testing in order to demonstrate the generalization of the method. The image and VF quality criteria were used only for the purpose of selecting reliable measurements and were not used in the modelling. Moreover, the proposed model does not need the initial labelling of the subject data as being from glaucomatous or healthy eyes, and under the Bayesian framework, no manual input parameters are required.

Statistical Models

What follows is a description of the principal methods and models developed. Technical and mathematical details can be found elsewhere²² and are reviewed in the Appendix. The BRBF model was developed and written in Matlab (version 7.4.0 R2007a, The MathWorks, Inc., Natick, MA). An executable version of this code is freely available from the authors.

We aimed to generate a model that will ‘map’ an individual structural measurement (RNFLT values from a software generated peripapillary profile or an individual RNFLT value at a pixel in the image) to a sensitivity (dB) value at an individual VF location. Such a model will

allow the prediction of a VF sensitivity value from RNFLT values and vice versa. The remaining part of this section compares the BRBF model to the linear model that has been used widely to assess the association between structural and functional measurements.

Starting with a linear model, consider the case where we attempt to predict an individual VF sensitivity value denoted \hat{y}_d (where d is one of the 52 locations in a 24-2 HFA VF) from a series of RNFLT values denoted x_i for i from 1 to m . This can be expressed by the following over-simplified but illustrative equation:

$$\hat{y}_d = \mathbf{w}_{d1}\mathbf{x}_1 + \mathbf{w}_{d2}\mathbf{x}_2 + \dots + \mathbf{w}_{dm}\mathbf{x}_m + c_d \quad (1)$$

where c_d is a constant offset. The symbol on \hat{y}_d indicates that it is a prediction rather than the real measured value denoted by y_d . In this example, the equation has 64 peripapillary thickness profile values ($m=64$) each with its own coefficient which quantifies the contribution of each x value to the prediction. So each y value can be predicted by a ‘linear combination’ of x values. With some actual data we can find some real numbers for the w terms by least squares regression; this attempts to ‘fit’ an equation that minimises the difference between the predicted and measured values. This yields an individual equation for each y that can be enumerated across all the points to predict a complete VF from a given vector of x values. This classic multiple linear regression can be adapted to select only those x values that are statistically significant for the prediction of y values using techniques such as stepwise multiple regression²³ with the forward selection scheme. In a linear model described by equation (1), the w values (divided by their standard errors) quantify the amount of meaningful contribution made by x values to predict the y values. The largest absolute w term (with respect to the variability in estimating the term) would indicate the x value that affects the y_d value the most, in the sense that change in this x value results in the largest change in y_d . Similarly, the next largest absolute w term would indicate the second most important term and so on. Equivalently, one could look at the relationship between the y_d value and each x value separately and simply calculate the correlation coefficient based on the raw data or on the ranks of the data (Spearman’s rho) and end up with a similar result. Loosely speaking this is the approach of Gardiner and colleagues,⁹ who used neuroretinal rim area estimated from scanning laser ophthalmoscope measurements (Heidelberg Retina Tomograph, Heidelberg Engineering, Heidelberg, Germany) as the surrogate structural measurement for glaucomatous damage. Particularly, in the linear model implemented for this study, the visual field sensitivity was ‘unlogged’ from the decibel value and the prediction

from this model was converted back to the decibel scale when compared with the measured sensitivity. We will refer to this method as a classic linear model.

This ‘classic linear model’ approach makes several restrictive and incorrect assumptions about the data. First it assumes that each x value is independent of all the other x values,²⁴ whereas in reality the x and y values are topographically and physiologically related and may interact as groups. Although one could try to demarcate these groups based on a physiological relationship between the x values, or an anatomical map, it would be preferable for the groups to be ‘learnt’ from the data rather than imposing any relationship from incomplete prior knowledge. Second, this approach assumes that the relationship between y and x is either linear or linear after some transform (typically logarithmic). In reality, the relationship between y and x may be more complex with the nature of the association probably changing across the measurement range of y . Put simply, at different stages of disease, the apparent relationship between y and x could switch from being linear, to noisy, to curvilinear and occasionally being censored due to the imprecision and range of the measurement. This notion that the association may change at different levels of functional loss was also asserted by published studies.^{25, 26} The third difficulty with the classic linear model is that outlier points exert an overly strong influence, and can yield a false association.

The RBF attempts to model the relationship between y and x without the limiting assumptions associated with the classic linear model described above. As an illustrative example, consider one x value, say x_1 , appearing to be co-related to a y value, say y_1 . This apparent relationship might be explained by x_1 being very strongly related to x_2 which in turn is very strongly associated with y_1 . Thus the apparent x_1 and y_1 relationship may well be much weaker or not even be significant. As it will be shown in the derived structure-function relationship (Figure 3-Figure 5), this covariance in the relationship between the y and x values is modelled better with the RBF approach. Furthermore, the central idea of the RBF are the basis functions, each of which performs very much like a dynamic window or kernel that moves across the data, both spatially and at various stages in disease severity, identifying groups of measurements that appear to behave in a similar pattern. The non-normalized Gaussian basis function used in this study has an activation field which has a centre: that is, a particular input value at which they have a maximal output. The output tails off as the input moves away from this point. In this way, those hidden basis functions that have centres similar to the input x patterns will have stronger activation and will thus contribute more to the prediction of y . On the other hand, those basis functions with weak activation will be

'isolated' and will not affect the prediction. Moreover, RBF 'learns' the parameters from the data and this is customised for our purpose by using a Bayesian framework (BRBF). The method makes predictions in multiple dimensions by extending the standard relevance vector machine²⁷ where the output is restricted to one dimension. The VF sensitivities at different locations are implicitly correlated by sharing the same basis functions and parameters of weights (See α in the Appendix). In the BRBF model, the original visual field sensitivity value in dB was used.

In general, BRBF is not restricted by the number of inputs in the model, or more precisely by the dimensionality of the data, so that it can be adapted to use the RNFLT values at each pixel, rather than only the 64-sector peripapillary thickness profile. In this study, examples of the SLP images used for predicting VF are shown in Figure 2. We used an annular region, centred on the ONH. The inner and outer diameters were 2.3mm and 4.9mm, respectively, so that the annulus was 26 pixels wide (compared with the 8-pixel calculation ring in the GDx software from which the 64-sector RNFLT peripapillary profile is computed). In this annulus, there are 16512 pixels each with a retardation value. We hypothesised that the predicted spatial structure-function relationships would be strengthened by avoiding the data reduction to 64 sector RNFLT values. This hypothesis will be validated by the improved structure-function relationship derived from the BRBF by using the measurement in its higher dimensional form.

Another challenge in the modelling process involves handling the large dimensionality of the SLP data. If the dimensionality M and the number of data points N of a dataset satisfy $M \geq N$, the dimensionality of the dataset can be reduced from M to $N-1$ with minimal loss of information using Principal Component Analysis²⁸ (PCA), because the N data points span at least one linear *hyperplane* in this M -dimensional space. Using this technique the 16512 dimensional SLP image vectors were reduced to 227 dimensions for analysis and transformed back to the original SLP vectors for the purpose of visualization and evaluation of results. Using the classic linear model on a reduced SLP image vector with 227 elements and a 24-2 VF with 52 sensitivity values will still result in a prohibitive number of 'weights' (11856) to be fitted, which will cause significant overfitting to the 'noise' in the data.

Testing the Model

It is well established that if validation of a modelled relationship between dependent and independent variables is performed on the same dataset as the selection of input variable and weights, then the model estimates will be overly optimistic^{29, 30}. It is also well known that in

developing a model, the input variables and weights selected may vary across different samples³¹. Therefore, the models were developed on the MEH and REH data alone, leaving the BMES data as a test dataset.

The predictive performance of the classic linear model and the BRBF was evaluated by point-by-point analysis of the predictions of the VF sensitivity in the 306 VFs from the BMES dataset. The predictive performance was summarised by the mean of the absolute prediction errors in the 52 points of the VF.

Matlab code was written to display the results and present the output of the linear and BRBF models via a graphical user interface. One graphical output was a structure-function map in a similar format to that described by Gardiner et al (2005).⁹ The structure-function relationship was defined by the corresponding functional change given a subtle structural change, which is mathematically modelled by the derivative of the BRBF (Appendix). This describes the relationship between y (VF sensitivity) and x (RNFLT) at each individual VF location. The other output from this analysis consisted of point-by-point predictions of each subject's VF as represented by the HFA greyscale (which was replicated for this purpose). These outputs were considered for 1) the classic linear model, 2) the BRBF I model (based on the 64 summary RNFLT values output from the GDx software) and 3) for the BRBF II model (based on the reduced 227 dimensional data derived from the PCA on the 16512 individual pixel retardation values in the broad annulus centred on the ONH).

Results

A summary of the measurements: HFA mean deviation (MD), HFA pattern standard deviation (PSD); GDx Nerve Fibre Indicator (NFI)) for each of the datasets is given in Table 1.

The mean absolute prediction error of VF sensitivities in the 306 eyes from the BMES data was 4.9dB (standard deviation (SD) 4.0dB) for the classic linear model. In comparison, both BRBF models yielded a nearly two-fold improvement ($P < 0.001$; paired t-test) in performance: BRBF I 2.9dB (SD 3.7dB), BRBF II 2.8dB (SD 3.8dB). In BRBF I and BRBF II models, the training process described in Appendix selected 49 and 73 basis functions respectively in the hidden layer.

Figure 1 summarises the predictive performance of the classic linear model and the BRBF I model across the range of VF sensitivity measurements. The BRBF II demonstrated similar prediction performance as BRBF I. Published test-retest differences (5th and 95th percentile

limits)³² across all locations from two VF tests from each of 49 individuals have been superimposed on Figure 1b. On inspection, these limits are similar to the 90% prediction limits when using the BRBF to predict the VF from a GDx RNFLT measurement of the same individual. Note that predictions at higher sensitivities (>30dB) tend to be slightly lower than the actual values whilst at lower sensitivities (<20dB) the predictions tend to be higher.

Figure 2 gives some case examples of the predictions. In some cases, the classic linear model overestimates the defect severity of the VF (I and III) and in other cases predicts a less damaged VF (IV), when compared to the true measured VF. In Figure 2(II) the classic linear model matches the overall average sensitivity of the VF but fails to capture the spatial location of this loss. In each case the BRBF better estimates the true VF, with spatial features of the measured defects generally retained. In Figure 2(IV) the BRBF model manages to predict the advanced defect severity.

Figures 3, 4 and 5 provide topographical maps of the spatial relationship between RNFLT positions on the peripapillary annulus and VF sensitivity at all the points in the VF, by means of classic linear regression, BRBF I and BRBF II, respectively. The agreement between the derived structure-function relationship and the anatomical benchmark was also summarised by calculating the absolute angular difference between the direction with the strongest derived relationship and the anatomical benchmark. This was calculated as the median of the absolute angular difference across all locations in a spatial relationship map such as Figures 3, 4 and 5. Both visual inspection on the spatial relationship and the quantified agreement with anatomical prior knowledge showed that the structure-function relationship derived by the classic linear regression model (Figure 3) has little concordance (median absolute angular difference of 62°) with the anatomical benchmark.³³ This correspondence improves ($P < 0.001$; paired t-test) with the BRBF I model (median absolute angular difference of 15°) in general, and improves further ($P < 0.001$; paired t-test) still with the BRBF II model (median absolute angular difference of 12°), especially at the points around central vision and blind spot. This is consistent with the BRBF models learning to 'encode' the structure-function relationship during the training.

Discussion

The application of ANNs to both functional and structural measurements in glaucoma is not a new idea.³⁴⁻⁴⁰ Most of these applications have tended to use a 'conventional' MLP ANN. Technically there are several advantages of the RBF over MLP ANNs. For example, with the latter there is an input and the distributed pattern 'lights up' all hidden units to contribute to

the prediction of the output, which makes them combine and interfere with each other. This typically yields a highly non-linear training process with mathematical difficulties that result in a slow convergence of a training procedure¹⁶. Moreover, the complexity of hidden unit patterns causes difficulty when interpreting the result because the connection among units and the hidden unit output do not have any physical or realistic meaning: they are simply some numbers that can produce a correct output. Hence, MLP ANNs are less suitable for the mapping of points in different measurement spaces, which requires a detailed understanding of the hidden layer output and other manipulation (e.g. derivatives) within the network. In this study, although an MLP provided a prediction accuracy comparable to the BRBF (data not shown), the spatial aspects of the structure/function relationship were poorly predicted. This likely results from complex interactions among the large number of weights in the MLP model. In contrast, RBF substitutes hidden layers in MLP with a set of basis functions, which leaves the solution of weights in a linear space. The Gaussian basis function forms a local representation in the hidden unit, each of which can be understood as a representative of similar input patterns (Figure 2). With a given RNFLT input, only a few ‘representatives’ will be activated and contribute to the VF prediction (Figure 2). Furthermore, the RBF handled within a Bayesian probabilistic framework,²⁷ as developed for our purposes, is unlike most other ANN approaches because it is independent of any subjective input parameter, and thus requires no model validation on a test dataset provided that the training dataset is representative and sufficiently large to enable modelling of the many different states of the VF. However, for this study the ‘trained’ model is still tested on a separate, independent dataset to illustrate the generalisation of the model performance. One ‘technical’ limitation of the current BRBF model, despite its good performance, is that it assumes that the variability in the VF measurements is largely Gaussian, which is not optimal given that it is often skewed and heavily-tailed.³²

VF locations have previously been related to sectors of the ONH using an anatomical map³³ derived by overlaying an appropriately scaled VF grid on RNFL photographs and tracing nerve fibre bundles or defects from various VF locations to the ONH margin. Gardiner and colleagues⁹ produced a topographical map of the relationship between sectors of the ONH and locations in the VF by considering the linear correlation between Heidelberg retina tomography neuroretinal rim area and VF sensitivity at each point in the VF. The classic linear model is akin to that derived by Gardiner et al except that the SLP measurements from GDx imaging are used. The maps derived from the BRBF (Figures 4 and 5) indicate a closer concordance with the anatomically derived landmark than the map derived from the classic linear model (Figure 3). In addition, the predictions on pointwise VF sensitivities in the validation dataset were, on average, better for the BRBF method than the classic linear model.

A plausible explanation for the improvements afforded by the BRBF technique is that it models the spatial and quantitative structure-function relationship more precisely. The technical and statistical advantages of the BRBF model over the classic linear model would support this notion. For example, the BRBF considers that the VF points, and indeed RNFLT values acquired from different discrete areas, interact as groups rather than as independent measurements. The BRBF also accommodates the covariance and non-independence of the measurements; it is less affected by outlying observations and makes no assumption about the linearity of relationships. Of course, one difficulty in generating any type of map, driven by data or anatomical observation, is the restriction in the sampling of VF points: these are, for example, probably not optimally placed for estimating RGC density nearer the fovea.

The range and distribution of differences between the measured VF sensitivity values and those predicted from the RNFLT by the BRBF, at different levels of sensitivity, is shown in Figure 1b. This profile is remarkably similar to published limits for test retest variability when two VFs are measured within a short space of time.³² This suggests that, on average, a VF predicted by the BRBF from RNFLT values has measurement noise equivalent to that found in a newly measured field. This isn't as exciting as it may first appear because it is well established that the measurement noise in VFs is already very high, prohibiting straightforward clinical diagnosis of glaucomatous defects and monitoring progression. Nevertheless, this finding illustrates that the range and scale of the average predictive performance of the BRBF model is much better than the classic linear model approach, which completely fails to predict the full range of VF values (Figure 1a).

Although the mean absolute prediction error is reduced with BRBF I and BRBF II, the standard deviation of the absolute prediction error of both BRBF models are still large (3.7dB and 3.8dB). This can also be observed in more detail in the prediction limits shown in Figure 1(b). Despite of the general similarity between the prediction limits and VF test-retest limits, predictions at the normal end of the range still tend to be lower than the actual VF measurements, and at the damaged end, predictions tend to be higher than actual VF measurements. The reported retest differences,³² on average, are very small at the normal or 'healthy' end. At the damaged end, the retest values tend to be higher, but the median BRBF predictions are a little higher than the retest values. This likely reflects the difficulty the prediction from RNFLT images have in identifying small, focal defects. Moreover, the 'floor effect' in the VFs and GDxVCC SLP images^{41, 42} and the atypical scan pattern in GDxVCC SLP images, which may be associated with glaucoma severity,⁴³ may be additional causes of the overestimation at the lower end of the VF sensitivity. Furthermore, because the diagnosis of subjects in REH datasets includes structural criteria, the normal subjects in the training

dataset may have ‘super-normal’ structure and the glaucomatous subjects have greater than average structural damage. This potential bias on subject selection might distort the structure-function relationship. Therefore, the training process may be improved by including a range of glaucoma severity in subjects defined only by VF loss. Another factor that may confound the reported prediction accuracy is that the models were trained with VFs tested with both SITA and full-threshold programs, while they were evaluated on VFs tested only with full-threshold program. This may, in part, account for the observed tendency for the prediction to overestimate the sensitivities in the test dataset due to the higher sensitivities obtained with SITA compared with the full-threshold program.⁴⁴ However, this effect would be small because the sensitivity difference with two programs is just 1.3dB on average.⁴⁴

Recent investigations attempting to uncover the structure-function relationship in glaucoma generally have the aim of assessing the relative accuracy of structural and functional tests throughout the course of the disease^{45, 46}. For example, loss of function without loss in structure that does not adhere to a particular structure-function model’s prediction might be an indicator of a non-glaucomatous process, measurement imprecision, or some artefact in the image of the structure or function test. Our long term aim is to use the BRBF technique to provide a relevant clinical tool that indicates concordance between the VF and the chosen surrogate measure for structural loss. For example, when a VF and structural measure derived from one of GDx, HRT or optical coherence tomography (OCT) is available, a chart mapped in VF space will be provided indicating areas where the measurements are in concordance (within a certain range of accuracy and precision) and where they are not: this could provide clinically useful information about the reliability of the individual measurements or diagnostically useful information.

It is an imperative that any new statistical method should be developed and tested on more than one dataset.³⁰ We had access to three large independent datasets, each collected at one of three clinical centres. The inclusion criteria for glaucomatous and healthy subjects were generally consistent across the three samples. However, as the aim of this study was not to determine diagnostic performance, the precise definitions for glaucoma were less important. In fact, the mixture of data can be viewed as an advantage in the study design. However, further testing on different datasets, especially where realistic estimates of measurement precision have been performed (from test-retest measurement), is still required and this is being undertaken in our laboratory and elsewhere.

The BRBF method is not limited to one type of input of structural measurement or imaging device. The BRBF was shown to handle input of the GDx RNFLT peripapillary profile (64

values) as well as the PCA-reduced RNFLT values at 16512 pixels in a wide peripapillary annulus. The BRBF method could be used on neuroretinal rim area values from SLO technology or RNFLT values derived from OCT technology, or any other surrogate measure of glaucomatous structural loss. Moreover, we have demonstrated, albeit qualitatively with the maps in Figure 5, that using the surrogate measures of RNFLT in their high dimensional form provides a closer mapping to the expected structure-function relationship. We speculate that the next generation of Fourier domain OCT instrumentation, now finding its way into clinics and providing volumes of data for RNFLT, will be particularly amenable to this method.

In conclusion, we have introduced a new statistical method for describing the relationship between functional and structural measurements used in the clinical evaluation of glaucoma. Evidence from a dataset independent of those used to derive the model indicates that the BRBF method has advantages over standard statistical approaches for modelling these relationships, and estimates of functional deficits from structural measures yielded from this method are better than those derived from a classic linear regression approach. This method can provide a platform from which clinically useful tools can be derived for mapping and charting concordance between VF measurements and RNFLT measurements in glaucoma.

Appendix

Our proposed method to link the structural and functional measurements is formalized by a function \mathcal{G} , which would predict functional measurement \mathbf{y} from a structural one \mathbf{x} : $\mathbf{y} = \mathcal{G}(\mathbf{x})$. This sets a mathematical framework for the question: what would be the corresponding functional change ($\Delta\mathbf{y}$) for the structural change $\Delta\mathbf{x}$: $\Delta\mathbf{y} = \mathcal{G}(\mathbf{x} + \Delta\mathbf{x}) - \mathcal{G}(\mathbf{x})$? Because we are interested in subtle structural change to model the slow progression of RNFLT damage, we assume that $\Delta\mathbf{x}$ becomes very small and tends to 0. The structure-function relationship is then defined with the general equation:

$$\lim_{\Delta\mathbf{x} \rightarrow 0} \frac{\Delta\mathbf{y}}{\Delta\mathbf{x}} = \lim_{\Delta\mathbf{x} \rightarrow 0} \frac{\mathcal{G}(\mathbf{x} + \Delta\mathbf{x}) - \mathcal{G}(\mathbf{x})}{\Delta\mathbf{x}} = \nabla_{\mathbf{x}} \mathcal{G} \quad (2)$$

where \mathcal{G} is differentiable w.r.t. \mathbf{x} , and $\nabla_{\mathbf{x}} \mathcal{G}$ is the gradient of \mathcal{G} at \mathbf{x} . Since we are sampling subjects rather than considering the whole population, the final term in this equation must be expressed as a statistical expectation of $\nabla_{\mathbf{x}} \mathcal{G}$ or, for simplicity, the mean of $\nabla_{\mathbf{x}} \mathcal{G}$.

We examined classic linear regression and BRBF as the choice of function \mathcal{G} . The latter was extended from the Relevance Vector Machine (RVM),²⁷ where the output is originally only

one-dimensional. The extension was similar to the model derived by Thayanathan et al (2006).⁴⁷ In particular, VF sensitivity is assumed to be:

$$\mathbf{y}_d^n = \mathbf{w}_d^T \phi(\mathbf{x}^n) + \varepsilon_d \quad (3)$$

where \mathbf{y}_d^n is the d th element in the measurement of the n th subject, \mathbf{x}^n is the RNFLT measurement (64-point profile or SLP image) vector, \mathbf{w}_d is a weight vector, ε_d is an additive zero-mean Gaussian noise $\mathcal{N}(0, \delta_d^2)$ with variance δ_d^2 , and the radial basis function vector $\phi(\mathbf{x}^n)$ is defined to be $M+1$ dimensional for M bases: $\phi(\mathbf{x}^n) = (1, \phi_1(\mathbf{x}^n), \phi_2(\mathbf{x}^n), \dots, \phi_M(\mathbf{x}^n))^T$, where each element is a radial basis function with centre θ_m and an isotropic covariance:

$$\phi_m(\mathbf{x}^n) = \exp\left(-\eta_m (\mathbf{x}^n - \theta_m)^T (\mathbf{x}^n - \theta_m)\right) \quad (4)$$

If all weight vectors \mathbf{w}_d are organized into a matrix \mathbf{W} columnwise, then using Bayesian methodology we assign a prior over \mathbf{W} :

$$\mathbf{w}_d \sim \mathcal{N}(0, \Psi) \quad \text{and} \quad p(\mathbf{W} | \Psi) = \prod_d \mathcal{N}(0, \Psi) \quad (5)$$

where Ψ is a diagonal matrix whose elements are $\alpha_1^{-1}, \alpha_2^{-1}, \dots, \alpha_M^{-1}$ on diagonal and 0 otherwise. Each α_m^{-1} represents the average variance of the weights for the m th basis.

According to Bayesian methodology, priors of hyper-parameters are defined over α_m and $\beta_d = \delta_d^{-2}$:

$$p(\alpha) = \prod_m \text{Gamma}(\alpha_m | a, b), \quad p(\beta) = \prod_d \text{Gamma}(\beta_d | c, d) \quad (6)$$

where \mathbf{a} and \mathbf{b} are vectors of α_m and β_d respectively, and $\text{Gamma}(\alpha_m | a, b)$ is a Gamma distribution with parameters a and b .

The framework above forms the objective function, which is the probability of all parameters, $\mathbf{W}, \mathbf{a}, \mathbf{b}$, given the observations \mathbf{Y} :

$$p(\mathbf{W}, \mathbf{a}, \mathbf{b} | \mathbf{Y}) = p(\mathbf{W} | \mathbf{Y}, \mathbf{a}, \mathbf{b}) p(\mathbf{a}, \mathbf{b} | \mathbf{Y}) \quad (7)$$

where \mathbf{Y} is a matrix, the columns of which are \mathbf{y}^n for n from 1 to N .

In the first item in equation (7), it is straightforward to infer that \mathbf{w}_d is independent from any other weight vectors given \mathbf{Y} , $\boldsymbol{\alpha}$ and $\boldsymbol{\beta}$. Consequently:

$$p(\mathbf{W} | \mathbf{Y}, \boldsymbol{\alpha}, \boldsymbol{\beta}) = \prod_d \frac{p(\mathbf{y}_d | \mathbf{w}_d, \beta_d) p(\mathbf{w}_d | \boldsymbol{\alpha})}{p(\mathbf{y}_d | \boldsymbol{\alpha}, \beta_d)} = \prod_d \mathcal{N}(\mu_{\mathbf{w}_d}, \Sigma_{\mathbf{w}_d}) \quad (8)$$

where the covariance matrix and mean for the posterior distribution of \mathbf{w}_d are:

$$\Sigma_{\mathbf{w}_d} = (\beta_d \Phi(\mathbf{X})^T \Phi(\mathbf{X}) + \Psi^{-1})^{-1} \quad \text{and} \quad \mu_{\mathbf{w}_d} = \beta_d \Sigma_{\mathbf{w}_d} \Phi(\mathbf{X})^T \mathbf{y}_d \quad (9)$$

where $\Phi(\mathbf{X})$ is a matrix: $\Phi(\mathbf{X}) = (\phi(\mathbf{x}^1), \dots, \phi(\mathbf{x}^N))^T$.

The latter item in equation (7) can be calculated as: $p(\boldsymbol{\alpha}, \boldsymbol{\beta} | \mathbf{Y}) \propto p(\mathbf{Y} | \boldsymbol{\alpha}, \boldsymbol{\beta}) p(\boldsymbol{\alpha}) p(\boldsymbol{\beta})$, where

$$\begin{aligned} p(\mathbf{Y} | \boldsymbol{\alpha}, \boldsymbol{\beta}) &= \int p(\mathbf{Y} | \mathbf{W}, \boldsymbol{\beta}) p(\mathbf{W} | \boldsymbol{\alpha}) d\mathbf{W} \\ &= \int \dots \int \prod_{\mathbf{w}_1, \mathbf{w}_D} \prod_d p(\mathbf{y}_d | \mathbf{w}_d, \beta_d) p(\mathbf{w}_d | \boldsymbol{\alpha}) d\mathbf{w}_1 \dots d\mathbf{w}_D \\ &= \prod_d \mathcal{N}(0, \beta_d^{-1} I + \Phi(\mathbf{X}) \Psi \Phi(\mathbf{X})^T) \end{aligned} \quad (10)$$

With no prior knowledge on $\boldsymbol{\alpha}$ and $\boldsymbol{\beta}$, these two parameters are assumed to be ‘‘uniformly’’ distributed so $p(\boldsymbol{\alpha})$ and $p(\boldsymbol{\beta})$ have little impact on $p(\boldsymbol{\alpha}, \boldsymbol{\beta} | \mathbf{Y})$. Using the similar approximation as that of RVM,²⁷ the hyper-parameters are optimized by setting the derivative of equation (10) to be zero:

$$\alpha_m = \frac{D}{\sum_d ((\mu_{\mathbf{w}_d}^m)^2 + \Sigma_{\mathbf{w}_d}^{mm})} \quad \text{and} \quad \beta_d = \frac{N - \sum_m (1 - \alpha_m \Sigma_{\mathbf{w}_d}^{mm})}{(\mathbf{y}_d - \Phi(\mathbf{X}) \mu_{\mathbf{w}_d})^T (\mathbf{y}_d - \Phi(\mathbf{X}) \mu_{\mathbf{w}_d})} \quad (11)$$

where $\mu_{\mathbf{w}_d}^m$ is the m th element of the vector $\mu_{\mathbf{w}_d}$, and $\Sigma_{\mathbf{w}_d}^{mm}$ is the diagonal element at m th row and column in $\Sigma_{\mathbf{w}_d}$.

The parameters are inferred by iterating between equations (9) and (11) until convergence. The radial basis centres θ_m are initialized to contain all \mathbf{x}^n . As with an RVM, many of α_m

become infinite during the training process, so the corresponding radial bases are removed accordingly. The radial basis parameter η_m is optimized by gradient descent.

Given the inferred parameters, the distribution of predicted values \mathbf{y}'_d given a test example \mathbf{x}' is computed as:

$$\begin{aligned}
 & p(\mathbf{y}'_d | \mathbf{y}_d, \boldsymbol{\alpha}, \boldsymbol{\beta}) \\
 &= \int p(\mathbf{y}'_d | \mathbf{w}_d, \boldsymbol{\beta}) p(\mathbf{w}_d | \mathbf{y}_d, \boldsymbol{\alpha}, \boldsymbol{\beta}) d\mathbf{w}_d \\
 &= \mathcal{N}(\boldsymbol{\mu}_{\mathbf{w}_d}^\top \boldsymbol{\phi}(\mathbf{x}'), \boldsymbol{\beta}_d^{-1} + \boldsymbol{\phi}(\mathbf{x}')^\top \boldsymbol{\Sigma}_{\mathbf{w}_d} \boldsymbol{\phi}(\mathbf{x}'))
 \end{aligned} \tag{12}$$

where the prediction is made by the mean of the distribution: $\boldsymbol{\mu}_{\mathbf{w}_d}^\top \boldsymbol{\phi}(\mathbf{x}')$.

Therefore, the structure-function relationship in equation (2) is implemented by

$$\boldsymbol{\mu}_{\mathbf{w}_d}^\top \frac{\partial \boldsymbol{\phi}(\mathbf{x}^n)}{\partial \mathbf{x}^n} \tag{13}$$

where $\frac{\partial \boldsymbol{\phi}(\mathbf{x}^n)}{\partial \mathbf{x}^n} = \left(\frac{\partial \phi_1(\mathbf{x}^n)}{\partial \mathbf{x}^n}, \dots, \frac{\partial \phi_M(\mathbf{x}^n)}{\partial \mathbf{x}^n} \right)^\top$, and $\frac{\partial \phi_m(\mathbf{x}^n)}{\partial \mathbf{x}^n}$ is a vector: $-2\eta_m \phi_m(\mathbf{x}^n)(\mathbf{x}^n - \boldsymbol{\theta}_m)$ according to equation (4).

1. Anderson RS. The psychophysics of glaucoma: Improving the structure/function relationship. *Prog Ret Eye Res* 2006;25:79-97
2. Brigatti L, Caprioli J. Correlation of visual field with scanning confocal laser optic disc measurements in glaucoma. *Arch Ophthalmol* 1995;113(9):1191-1194.
3. Weinreb RN, Shakiba S, Sample PA, et al. Association between quantitative nerve fiber layer measurement and visual field loss in glaucoma. *Am J Ophthalmol* 1995;120:732-738.
4. Iester M, Mikelberg FS, Courtright P, Drance SM. Correlation between the visual field indices and Heidelberg retina tomograph parameters. *J Glaucoma* 1997;6(2):78-82.
5. Teesalu P, Vihanninjoki K, Airaksinen P, Tuulonen A, Laara E. Correlation of blue-on-yellow visual fields with scanning confocal laser optic disc measurements. *Invest Ophthalmol Vis Sci* 1997;38:2452-2459.
6. Garway-Heath DF, Holder GE, Fitzke FW, Hitchings RA. Relationship between Electrophysiological, Psychophysical, and Anatomical Measurements in Glaucoma. *Invest Ophthalmol Vis Sci* 2002;43:2213-2220.
7. Garway-Heath DF, Viswanathan A, Westcott M. Relationship between perimetric light sensitivity and optic disc neuroretinal rim area. In: Wall M, Wild JM (eds), *Perimetry Update 1998/1999*. The Netherlands: Kugler Publications The Hague; 1999:381-389.
8. Anton A, Yamagishi N, Zangwill L, Sample P, Weinreb R. Mapping structural to functional damage in glaucoma with standard automated perimetry and confocal scanning laser ophthalmoscopy. *Am J Ophthalmol* 1998;125(4):436-446.
9. Gardiner SK, Johnson CA, Cioffi GA. Evaluation of the Structure-Function Relationship in Glaucoma. *Invest Ophthalmol Vis Sci* 2005;46:3712-3717.
10. Mai TA, Reus NJ, Lemij HG. Structure-Function Relationship Is Stronger with Enhanced Corneal Compensation than with Variable Corneal Compensation in Scanning Laser Polarimetry. *Invest Ophthalmol Vis Sci* 2007;48:1651-1658.
11. Bowd C, Zangwill LM, Medeiros FA, et al. Structure and Function in Glaucoma: The Relationship between a Functional Visual Field Map and an Anatomic Retinal Map. *Invest Ophthalmol Vis Sci* 2006;47:2889-2895.
12. Schlottmann PG, Cilla SD, Greenfield DS, Caprioli J, Garway-Heath DF. Relationship between Visual Field Sensitivity and Retinal Nerve Fiber Layer Thickness as Measured by Scanning Laser Polarimetry. *Invest Ophthalmol Vis Sci* 2004;45:1823-1829.
13. Powell MJD. Radial basis functions for multivariate interpolation: A review. In: Mason JC, Cox MG (eds), *Algorithms for the approximation of functions and data*. Clarendon Press; 1987:143-167.
14. Orr MJL. Introduction to Radial Basis Function Networks. 1996.
15. Poggio T, Girosi F. Networks for approximation and learning. *Proceedings of the IEEE* 1990;78:1481-1497.
16. Bishop CM. *Neural network for pattern recognition*: Oxford University Press; 1996.

17. Reus NJ, Lemij HG. Relationships between Standard Automated Perimetry, HRT Confocal Scanning Laser Ophthalmoscopy, and GDx VCC Scanning Laser Polarimetry. *Invest Ophthalmol Vis Sci* 2005;46:4182-4188.
18. Keltner JL, Johnson CA, Cello KE, et al. Classification of visual field abnormalities in the ocular hypertension treatment study. *Arch Ophthalmol* 2003;121:643-650.
19. Mitchell P, Smith W, Attebo K, Healey PR. Prevalence of open-angle glaucoma in Australia. The Blue Mountains Eye Study. *Ophthalmology* 1996;103:1661-1669.
20. Greenfield D. Optic nerve and retinal nerve fiber layer analyzers in glaucoma. *Curr Opin Ophthalmol* 2002;13:68-76.
21. Reus NJ, Colen TP, Lemij HG. Visualization of localized retinal nerve fiber layer defects with the GDx with individualized and with fixed compensation of anterior segment birefringence. *Ophthalmology* 2003;110:1512-1516.
22. Zhu H, Crabb DP, Garway-Heath DF. A Bayesian Radial Basis Function Model to Link Retinal Structure and Visual Function in Glaucoma. *The 3rd International Conference of Bioinformatics and Biomedical Engineering*. Beijing: IEEE; 2009:1-4.
23. Hocking RR. The analysis and selection of variables in linear regression. *Biometrics* 1976;32:1-49.
24. Cohen J. Multiple Regression as a general data-analytic system. *Psychological Bulletin* 1968;70:426-443.
25. Harwerth RS, Carter-Dawson L, Smith EL, Crawford ML. Scaling the structure-function relationship for clinical perimetry. *Acta Ophthalmol Scand* 2005;83:448-455.
26. Gonzalez-Hernandez M, Pablo LE, Armas-Domingue K, Vega RR, Ferreras A, Rosa MG. Structure-function relationship depends on glaucoma severity. *Br J Ophthalmol* 2009;Epub ahead of print.
27. Tipping ME. The Relevance Vector Machine. In: Solla SA, Leen TK, Muller KR (eds), *Advances in Neural Information Processing Systems*: MIT Press; 2000:652-658.
28. Jolliffe IT. *Principal Component Analysis*: Springer Press; 1986.
29. Copas JB. Regression, prediction and shrinkage (with discussion). *J Roy Stat Soc B Met* 1983;45:311-354.
30. Altman DG, Royston P. What do we mean by validating a prognostic model. *Statistics in Medicine* 2000;19:453-473.
31. Miller AJ. Selection of subsets of regression variables (with discussion). *J Roy Stat Soc A Sta* 1984;147:389-425.
32. Artes PH, Iwase A, Ohno Y, Kitazawa Y, Chauhan BC. Properties of Perimetric Threshold Estimates from Full Threshold, SITA Standard, and SITA Fast Strategies. *Invest Ophthalmol Vis Sci* 2002;43:2654-2659.
33. Garway-Heath DF, Poinoosawmy D, Fitzke FW, Hitchings RA. Mapping the visual field to the optic disc in normal tension glaucoma eyes. *Ophthalmology* 2000;107:1809-1815.

34. Bowd C, Chan K, Zangwill LM, et al. Comparing Neural Networks and Linear Discriminant Functions for Glaucoma Detection Using Confocal Scanning Laser Ophthalmoscopy of the Optic Disc. *Invest Ophthalmol Vis Sci* 2002;43:3444-3454.
35. Goldbaum MH, Sample PA, White H, et al. Interpretation of automated perimetry for glaucoma by neural network. *Invest Ophthalmol Vis Sci* 1994;35:3362-3373.
36. Bengtsson B, Bizios D, Heijl A. Effects of Input Data on the Performance of a Neural Network in Distinguishing Normal and Glaucomatous Visual Fields. *Invest Ophthalmol Vis Sci* 2005;46:3730-3736.
37. Brigatti L, Hoffman D, Caprioli J. Neural networks to identify glaucoma with structural and functional measurements. *Am J Ophthalmol* 1996;121:511-521.
38. Uchida H, Brigatti L, Caprioli J. Detection of structural damage from glaucoma with confocal laser image analysis. *Invest Ophthalmol Vis Sci* 1996;37:2393-2401.
39. Brigatti L, Nouri-Mahdavi K, Weitzman M, Caprioli J. Automatic detection of glaucomatous visual field progression with neural networks. *Arch Ophthalmol* 1997;115:725-728.
40. Spenceley SE, Henson DB, Bull DR. Visual field analysis using artificial neural networks. *Ophthalmic and Physiological Optics* 2007;14:239-248.
41. Wyatt HJ, Dul MW, Swanson WH. Variability of visual field measurements is correlated with the gradient of visual sensitivity *Vision Research* 2007;47:925-936.
42. Blumenthal EZ, Horani A, Sasikumar R, Garudadri C, Udaykumar A, Thomas R. Correlating Structure With Function in End-Stage Glaucoma. *Ophthalmic Surg Lasers Imaging* 2006;37:218-223.
43. Yanagisawa M, Tomidokoro A, Saito H, et al. Atypical retardation pattern in measurements of scanning laser polarimetry and its relating factors. *Eye* 2009;23:1796-1801.
44. Sharma AK, Goldberg I, Graham SL, Mohsin M. Comparison of the Humphrey swedish interactive thresholding algorithm (SITA) and full threshold strategies. *Journal of glaucoma* 2000;9:20-27.
45. Hood DC, Anderson SC, Wall M, Kardon RH. Structure versus Function in Glaucoma: An Application of a Linear Model. *Invest Ophthalmol Vis Sci* 2007;48:3662-3668.
46. Hood DC, Kardon RH. A framework for comparing structural and functional measures of glaucomatous damage. *Prog Ret Eye Res* 2007;26:688-710.
47. Thayananthan A, Navaratnam R, Stenger B, Torr PHS, Cipolla R. Multivariate Relevance Vector Machines for Tracking. *Proceedings of the 9th European Conference on Computer Vision (ECCV '06)*. Graz, Austria; 2006:124-138.

	Subjects	Gender	Age mean \pm SD (min, max)	MD (dB) mean \pm SD (min, max)	PSD (dB) mean \pm SD (min, max)	NFI mean \pm SD (min, max)
MEH	Healthy	19M, 11F	40.6 \pm 15.6 (21, 75)	1.26 \pm 0.76 (0.09, 3.30)	1.47 \pm 0.28 (1.12, 2.27)	16 \pm 8 (2, 30)
	OHT	13M, 21F	60.7 \pm 11.1 (21, 75)	1.07 \pm 0.82 (0.10, 3.06)	1.35 \pm 0.27 (1, 2.1)	20 \pm 10 (5, 43)
	Glaucoma	28M, 15F	60.8 \pm 13.1 (31, 84)	-4.02 \pm 2.55 (-12.00, 1.15)	4.93 \pm 2.93 (1.49, 12.50)	42 \pm 18 (11, 80)
REH	Healthy	23M, 23F	60.4 \pm 12.1 (23, 77)	0.38 \pm 0.99 (-1.55, 2.73)	1.63 \pm 0.26 (1.13, 2.30)	21 \pm 9 (2, 43)
	Glaucoma	47M, 29F	62.2 \pm 10.1 (30, 82)	-9.52 \pm 8.43 (-30.39, 1.25)	8.35 \pm 4.32 (1.99, 15.92)	63 \pm 21 (21, 98)
BMES	Healthy	99M, 131F	69.3 \pm 6.5 (60, 87)	0.21 \pm 1.07 (-1.26, 3.03)	1.53 \pm 0.29 (1.12, 2.55)	19 \pm 10 (2, 49)
	Glaucoma	25M, 51F	72.0 \pm 6.3 (61, 78)	-7.94 \pm 6.55 (-29.67, 1.56)	6.97 \pm 3.76 (1.67, 15.56)	65 \pm 24 (27, 98)

Table 1: A summary of the measurements (HFA mean deviation (MD) and pattern standard deviation (PSD); GDx Nerve Fibre Indicator (NFI)) for the three datasets (MEH, REH, BMES) used in this study.

List of Figures

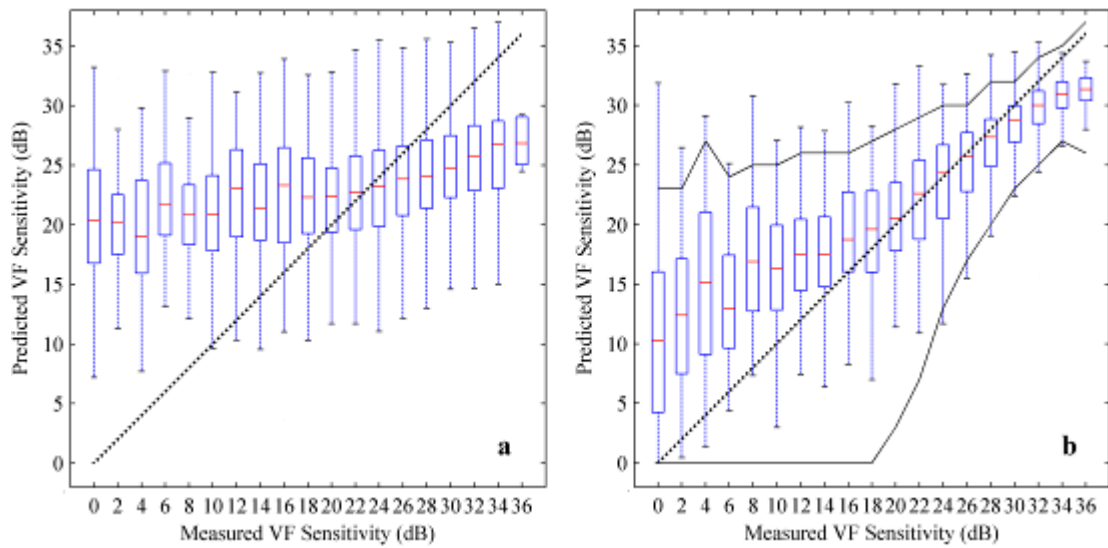


Figure 1. Distributions of the error between the predicted and the measured sensitivity for each visual field (VF) location in 306 eyes from the Blue Mountains Eye Study data, stratified by VF sensitivity. Each error bar summarises the predictive performance over a 2dB range from 0 to >36dB. Thin vertical lines indicate 90% prediction limits (5th and 95th percentile of error), the ‘boxes’ indicate the interquartile range of the prediction error (25th and 75th percentile error) with the line in the box indicates the median error. The dotted line of unity indicates perfect prediction (no error). (a) illustrates the predictive performance of the classic linear model. (b) illustrates the predictive performance of the Bayesian Radial Basis Function I model. Previously published (5th and 95th percentiles) test-retest limits³² for VF data derived from the pointwise differences between two VFs tested over a short period of time have been superimposed as black lines on (b).

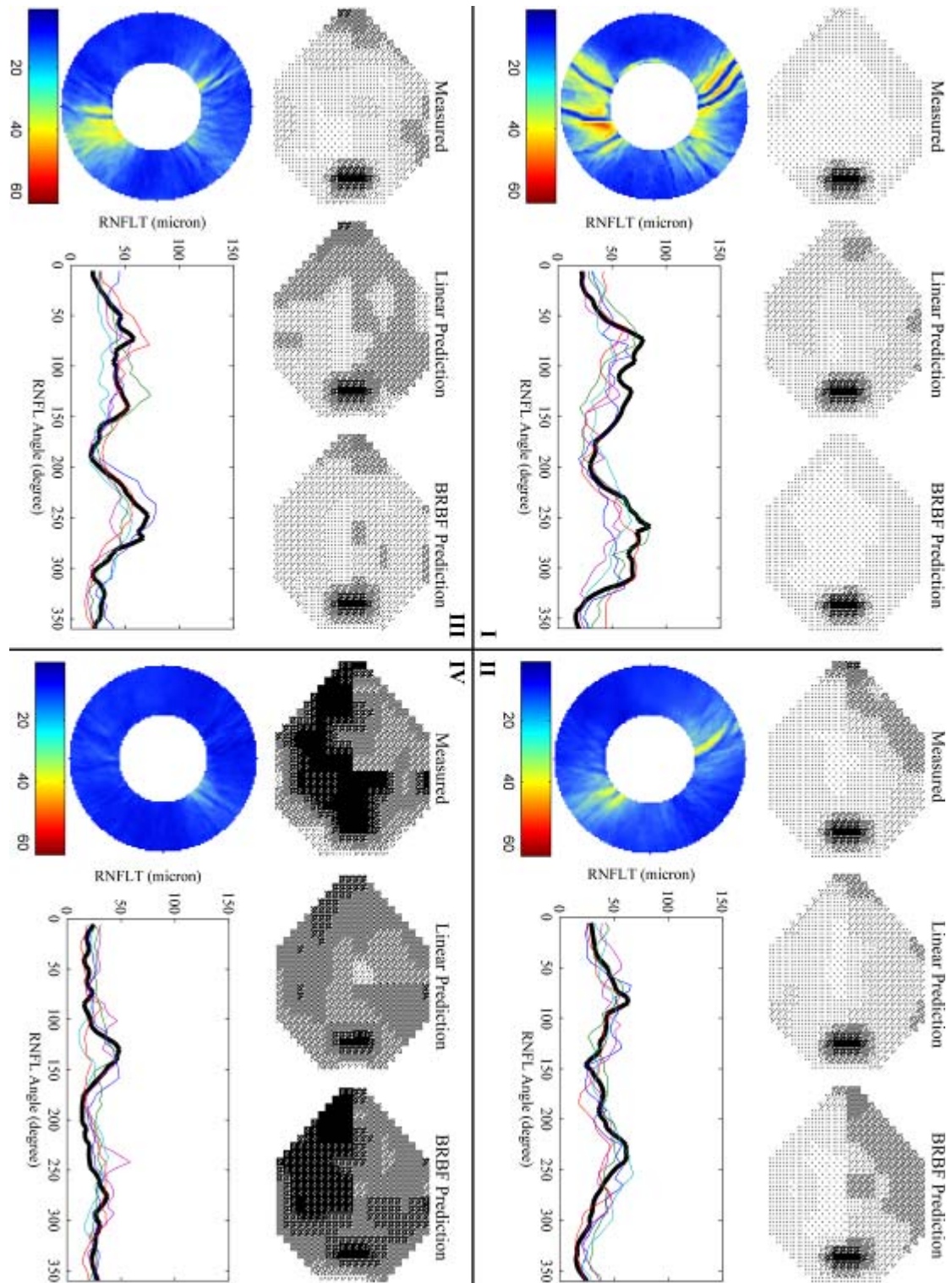


Figure 2. Model predictions for four cases from the Blue Mountains Eye Study dataset. For each case (I to IV), the top row shows, from left to right, Humphrey Field Analyzer visual field (VF) grayscales for the measured VF, the VFs predicted from the classic linear regression and the Bayesian Radial Basis Function (BRBF) with 64-sector retinal nerve fibre layer thickness (BRBF I), respectively. The predicted VF from BRBF II with 16512-pixel

annulus from the GDxVCC scanning laser polarimetry (SLP) images was in general similar to the one from BRBF I. The row of graphics below show the GDxVCC SLP image annulus and the corresponding 64-sector retinal nerve fibre layer thickness (RNFLT; thick black line) used to predict the VFs. The coloured lines in the 64-sector RNFLT plot indicate the top five radial basis functions with the strongest activation (those contributing the most to the prediction). More examples have been provided as supplementary material for this article.



Figure 3. A topographical map describing the relationship between the 64-sector retinal nerve fibre layer thickness (RNFLT) profile and individual VF (VF) locations as described by classic linear regression. The whole figure forms a Humphrey Field Analyzer 24-2 VF for a right eye. Each location is represented by a circular graph made up of 64 bars representing the correlation value between the VF location and the RNFLT at the corresponding angle. In this instance, the 'correlation values' are derived from scaled values of the weights given in equation (1). The length of the bar indicates the magnitude of the correlation, with red bars showing a positive correlation and blue bars indicating a negative correlation. The green bar with an asterisk indicates the location of expected strongest correlation on the basis of the anatomically derived map from Garway-Heath et al.³³



Figure 4. A topographical map describing the relationship between the retinal nerve fibre layer thickness (RNFLT) profile and individual VF points as described by Bayesian Radial Basis Function model I using the 64-sector RNFLT profile. The composition of the graph is the same as Figure 3 with the green bar with an asterisk indicates the location of expected strongest correlation on the basis of the anatomically derived map from Garway-Heath et al.³³ In this instance the 'correlation values' are derived from scaled values in equation (13).



Figure 5. A topographical map describing the relationship between the retinal nerve fibre layer thickness (RNFLT) profile and individual VF points as described by Bayesian Radial Basis Function model II using the 16512 pixel retardation values from the GDxVCC scanning laser polarimetry image. The composition of the graph is the same as Figure 3 and 4 with the green bar with an asterisk indicates the location of expected strongest correlation on the basis of the anatomically derived map from Garway-Heath et al.³³ In this instance the 'correlation values' are derived from scaled values in equation (13) and are summarized into 64 sectors for the purpose of comparison.